The Organization of Convection in Narrow Cold-Frontal Rainbands

G. W. KENT MOORE*

Geophysical Fluid Dynamics Program, Princeton University, Princeton, NJ 08540

(Manuscript received 10 July 1984, in final form 21 February 1985)

ABSTRACT

Narrow cold-frontal rainbands are lines of intense precipitation that straddle surface cold fronts. Recent observational work has revealed that the rainfall within the band is organized into regularly spaced ellipsoidal cells called precipitation cores. The rainband is coincident with a line of intense cyclonic shear associated with a low-level jet that lies ahead of and parallel to the surface cold front. Numerous authors have suggested that the organization of cells in the rainband is the result of shear instability of the horizontal wind field. To investigate this hypothesis, a linear stability analysis was performed on an idealized frontal zone consisting of a line of convection coincident with a line of cyclonic shear. To model the convective processes, the air inside the rainband was assumed to be unstably stratified. The presence of horizontal wind shear in an unstably stratified environment resulted in the existence of a mode with a short wave cutoff. The coupling between the convective processes and the shear instability in this mode was strong; its most unstable wave had properties similar to the precipitation cores observed in the narrow cold-frontal rainband.

1. Introduction

Recent observational work (Hobbs, 1978; Matejka *et al.*, 1980) has indicated that precipitation in extratropical cyclones is organized into two-dimensional structures called rainbands. The bands fall into two main categories: the wide-frontal rainbands that are oriented parallel to either the surface warm or cold front, and the narrow cold-frontal rainband that straddles the surface cold front. The narrow cold-frontal rainband is coincident with a line of strong cyclonic shear associated with a low-level jet that lies ahead of and parallel to the surface cold front. Embedded within these bands are smaller scale regions of intense rainfall called precipitation cores. In the wide bands, the cores are irregularly shaped and there is no discernible organization to them. The cores embedded within the narrow cold-frontal rainband are ellipsoidal in shape, are regularly spaced and have a definite orientation to the surface cold front.

James and Browning (1979) reported on the cellular structure of the narrow cold-frontal rainband. They found that the cells varied in length from a few kilometers to more than 100 kilometers and had lifetimes of 10 minutes to several hours. They stated that the cells were "oriented slightly clockwise with respect to the synoptic cold front." The passage of the narrow cold-frontal rainband was coincident with a windshift at the ground. The shear across the band was $\sim 5 \times 10^{-3}$ s^{-1}, the width of the shear zone was ~ 2.5 km and the depth of the convection was ~ 3 km. Hobbs and Biswas (1979) observed regularly spaced precipitation cores along the narrow cold-frontal rainband. They reported that the cores were oriented at an angle of $\sim 30°$ to the front and had a length of ~ 15 km. The cores were relatively shallow, penetrating to only 3–5 km. Hobbs and Persson (1982) observed a strong low-level jet with a maximum speed of 14 m s^{-1} coincident with the narrow cold-frontal rainband.

Carbone (1982) reported on the use of a triple Doppler radar network to study the passage of a cold front. The use of the three radars allowed him to deduce all components of the wind field independently. He did not have to make the assumption of two-dimensionality, as had been the case in earlier studies. For the cold front under study, he observed a band of intense precipitation 5 km wide and 250 km long coincident with a zone of strong cyclonic shear. Within 20 minutes, a disturbance with a wavelength of 13 km became noticeable in the band. The disturbance organized the precipitation into regularly spaced cores.

Parsons and Hobbs (1983) studied the life cycle of four narrow cold-frontal rainbands. They reported that in all cases the rainbands were associated with a windshift across the surface cold front and that the organization of the cores along the bands was similar. The authors described several cases in which a wide band moved across the surface front. This usually led to a decrease in the frontal convergence and resulted in a reduction in the organization of the narrow cold-frontal rainband. In cases where the interaction led to the elimination of the frontal convergence, the narrow cold-frontal rainband was observed to dissipate. In cases where it survived, the cores reformed. Initially there was little organization to them, but over a period of

* Present affiliation: Physics Department, University of Toronto, Toronto, Ontario, Canada M5S 1A7.

10–75 minutes the cores reorganized into a regular structure.

Hobbs and Persson (1982) noted that the circulation in the vicinity of the surface cold front was similar to that observed in laboratory studies of density currents. Due to frictional retardation at the lower boundary in these currents, the possibility exists that there will be an overhang of denser fluid over lighter fluid. The authors suggested that the precipitation cores are the analogues of these unstably stratified regions. However, in the absence of other processes, there would be no regular organization to these cores.

Numerous authors, including Emanuel (1980), Matejka (1980) and Carbone (1982), have suggested that the organization of convection in the narrow cold-frontal rainband is the result of shear instability across it. Barcilon and Drazin (1972) considered the coupling of barotropic Kelvin-Helmholtz and Rayleigh-Taylor instabilities in their study of dust devil formation. They considered the stability of a vertical vortex sheet in a fluid with a constant Brunt-Väisälä frequency. They found that coupling of the two instabilities resulted in very large growth rates; the most unstable waves, however, were those with the smallest horizontal scales. The lack of scale selection was attributed to the infinitesimal width of the shear layer. The analogous problem with a finite width shear layer was not considered.

Ross and Orlanski (1982) and Orlanski and Ross (1984) performed a numerical simulation of the evolution of a cold front over the southeastern United States. Their model included an explicit representation of the moist convective processes. This allowed the model to accurately simulate the interaction between the convective activity and the frontal scale flow. In cases without moisture present, the frontal zone was characterized by low-level convergence, a two-dimensional line vortex and a positive potential temperature anomaly. Inclusion of moisture intensified the frontal features; the maximum in the vorticity increased by ~70% and the temperature anomaly doubled. This was the result of more vigorous convection along the front. Of more interest was the cellular structure that developed in the moist case. The cells were evident in both the vorticity and temperature fields. The spacing of the cells was limited by the model grid spacing of 61.5 km. The cellular structure appeared to be the result of an interaction between the convective activity and the horizontal shear of the frontal scale flow.

In summary, observations and modeling studies have suggested that the organization of convection in the vicinity of surface fronts is the result of the strong horizontal shear of the background wind. An examination of the effects of shear on convection will be carried out in this paper.

2. Stability analysis of an idealized frontal zone

In this section, the stability of an idealized frontal zone to small amplitude perturbations will be considered. Implicit in this study is the assumption that there is a separation of the dynamics responsible for the frontal scale structure of the zone from those responsible for its cellular organization. The study will focus on the effects that horizontal wind-shear has on the convection at the front. This convection is the result of the strong convergence at the leading edge of the front. In keeping with the assumption of scale separation, this convergence is not explicitly treated. Instead it is considered to result in a band of air susceptible to convection. To model this convective activity, the air inside the band is assumed to be unstably stratified. The strong horizontal wind-shear is modeled by assuming that the velocity field parallel to the front is constant ahead of and behind this band and varies linearly across it. Thus the idealized frontal zone consists of a line of constant cyclonic shear coincident with a band of unstably stratified air. This idealization neglects the differences that exist between the pre- and post-frontal regions. Nevertheless, it is sufficient to capture the interaction of shear and convective instabilities present in the frontal zone. The model contains no microphysics and precipitation cores will be identified as regions where the waves have ascending motion. It should be noted that observations indicate that the regions of ascending motion have a vertical slant and as a result, the regions of precipitation are offset from them (Carbone 1982). The slant is undoubtedly due to vertical wind-shear, an effect not considered here. In Fig. 1, a schematic of the frontal zone is displayed. The six parameters that describe it are:

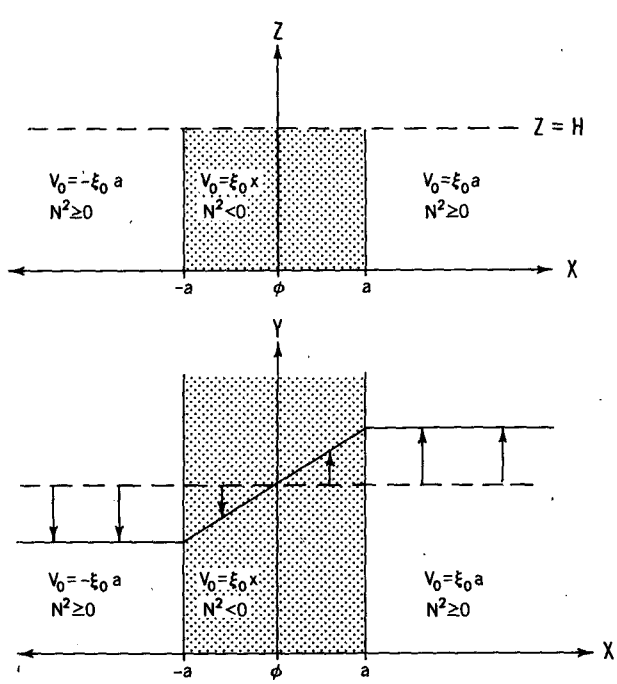

FIG. 1. Schematic of the vertical and horizontal cross sections through the idealized frontal zone. Stippled area denotes unstably stratified region.

ζ_0 the mean state vorticity (x-derivative of the mean state horizontal velocity field V_0),
N_1, N_3 the stable Brunt-Väisälä frequencies in the outer regions,
N_s the unstable Brunt-Väisälä frequency in the convective region,
$2a$ the width of the convective region and
H the depth of the convective region.

The linearization of the inviscid, incompressible equations of motion about the mean state described above yields:

$$\left.\begin{aligned}
&\frac{\partial U'}{\partial t} + V_0\frac{\partial U'}{\partial y} - f_0 V' = -\frac{1}{\rho_0}\frac{\partial P'}{\partial x}\\
&\frac{\partial V'}{\partial t} + V_0\frac{\partial V'}{\partial y} + (f_0+\zeta_0)U' = -\frac{1}{\rho_0}\frac{\partial P'}{\partial y}\\
&\frac{\partial W'}{\partial t} + V_0\frac{\partial W'}{\partial y} = -\frac{1}{\rho_0}\frac{\partial P'}{\partial z} - \frac{\rho' g}{\rho_0}\\
&\frac{\partial U'}{\partial x} + \frac{\partial V'}{\partial y} + \frac{\partial W'}{\partial z} = 0\\
&\frac{\partial \rho'}{\partial t} + V_0\frac{\partial \rho'}{\partial y} = \frac{\rho_0}{g}N^2 W'
\end{aligned}\right\}. \quad (3.1)$$

The depth of the convective region is assumed to be small compared to the scale height of the atmosphere and as a result ρ_0 and N^2 are independent of z.

The dynamic constraint that the perturbation pressure field is continuous and the kinematic constraint that the perturbation normal velocity is continuous are applied at the discontinuities of the mean state variables. To first order these reduce to:

$$\left.\begin{aligned}
P'(x=-a^-) &= P'(x=-a^+)\\
U'(x=-a^-) &= U'(x=-a^+)
\end{aligned}\right\}$$

and

$$\left.\begin{aligned}
P'(x=a^-) &= P'(x=a^+)\\
U'(x=a^-) &= U'(x=a^+)
\end{aligned}\right\}. \quad (3.2)$$

The boundary conditions in z are that the perturbation vertical velocity vanish at the surface and at the top of the convective region. That is,

$$\left.\begin{aligned}
W'(z=0) &= 0\\
W'(z=H) &= 0
\end{aligned}\right\}. \quad (3.3)$$

The linearized system (3.1) is separable in x and z. The separation will reduce it to a system of equations for the x-dependence of the perturbations and a vertical structure equation. I consider a normal mode expansion of the form:

$$\begin{vmatrix} U'(x,y,z,t)\\ V'(x,y,z,t)\\ P'(x,y,z,t)\\ W'(x,y,z,t)\\ \rho'(x,y,z,t)\end{vmatrix} = \mathrm{Re}\sum_l \begin{vmatrix} U_l(x)[W_z^*(z)/i\lambda]\\ V_l(x)[W_z^*(z)/i\lambda]\\ P_l(x)[W_z^*(z)/i\lambda]\\ W_l(x)W^*(z)\\ \rho_l(x)W^*(z)\end{vmatrix} e^{i(ly-\omega_l t)} \quad (3.4)$$

where

$[U_l, V_l, P_l, W_l P_l]$ are the complex-valued horizontal structure functions for the perturbation fields,
$[W^*, W_z^*]$ are the complex valued vertical structure function and its z-derivative,
l is the wavenumber parallel to the front,
λ is the separation constant (vertical wavenumber) and
ω_l is the complex frequency.

This yields an independent solution for each of the normal modes of the problem. For a given wavenumber l, the x-dependence of the perturbations satisfies:

$$\left.\begin{aligned}
&\Gamma U - f_0 V = -\frac{1}{\rho_0}P_x\\
&\Gamma V + n_0 U = -i\frac{l}{\rho_0}P\\
&\Gamma W = -i\frac{\lambda}{\rho_0}P - \frac{g}{\rho_0}\rho\\
&U_x + ilV + i\lambda W = 0\\
&\Gamma\rho = \frac{\rho_0}{g}N^2 W
\end{aligned}\right\}, \quad (3.5)$$

where

$$\left.\begin{aligned}
\Gamma(x) &= i(lV_0(x) - \omega)\\
\eta_0(x) &= f_0 + \zeta_0(x)\\
\xi_0(x) &= \frac{dV_0}{dx}
\end{aligned}\right\}.$$

The vertical structure equation is the same for all the wavenumbers and is

$$W_{zz}^* + \lambda^2 W^* = 0. \quad (3.6)$$

The boundary conditions in the vertical require that

$$\left.\begin{aligned}
W^*(0) &= 0\\
W^*(H) &= 0
\end{aligned}\right\}. \quad (3.7)$$

The solutions to (3.6) satisfying (3.7) are

$$W^*(z) = \sin\lambda_n z,$$

where

$$\lambda_n = n\pi/H,\ n = 0, 1, 2, \cdots.$$

The trivial solution $\lambda = 0$ reduces the problem to a

barotropic one in which W' and ρ' are zero and U', V' and P' are independent of z. This solution excludes any interaction between the shear and the convection and it will be discarded. I will consider the first vertical mode, that is the mode with only one maximum on $0 \leq z \leq H$. Therefore,

$$\lambda = \pi/H. \tag{3.8}$$

The character of the solutions is different in the interior and exterior regions. In the exterior, where the shear is zero, the problem can be solved in closed form. In the interior, with the exception of certain limiting cases, this is not possible. The interior and exterior solutions are coupled by the interface conditions (3.2) and these can be used to express the problem solely in terms of the x-dependence of the interior pressure perturbation. Details of this procedure can be found in Moore (1983) and results in the following:

$$P_{xx} - i\frac{2l\zeta_0\Gamma}{\Gamma^2 + f_0\zeta_0}P_x - \left[l^2\left(1 - \frac{2f_0\zeta_0}{\Gamma^2 + f_0\zeta_0}\right) + \lambda^2\left(\frac{\Gamma^2 + f_0\zeta_0}{\Gamma^2 - N_s^2}\right)\right]P = 0, \tag{3.9}$$

$$\left.\begin{aligned} P_x(-a) &= \kappa_1 P(-a) \\ P_x(a) &= -\kappa_3 P(a) \end{aligned}\right\}, \tag{3.10}$$

where

$$\kappa_1 = \left[\left(\frac{\Gamma_1^2 + f_0\eta_0}{\Gamma_1^2 + f_0^2}\right)K_1 + \frac{i}{\Gamma_1}\left(\frac{lf_0\zeta_0}{\Gamma_1^2 + f_0^2}\right)\right],$$

$$\kappa_3 = -\left[\left(\frac{\Gamma_3^2 + f_0\eta_0}{\Gamma_3^2 + f_0^2}\right)K_3 + \frac{i}{\Gamma_3}\left(\frac{lf_0\zeta_0}{\Gamma_3^2 + f_0^2}\right)\right],$$

$$\Gamma_1 = -i(l\xi_0 + \omega),$$

and

$$\Gamma_3 = i(l\xi_0 - \omega).$$

Thus the response of an idealized frontal zone to small amplitude perturbations has been reduced to the solution of the eigenvalue problem (3.9) and (3.10) for the complex frequency ω and eigenfunction P.

From the linearized system (3.1), one can show that the eddy kinetic and potential energy equations are

$$\frac{\partial}{\partial t}\iiint\left(\frac{U'^2 + V'^2 + W'^2}{2}\right)dxdydz = -\iiint\frac{g}{\rho_0}\rho'W'dxdydz - \iiint\zeta_0U'V'dxdydz$$

and

$$\frac{\partial}{\partial t}\iiint\left(\frac{1}{2}\frac{g^2}{\rho_0^2}\frac{\rho'^2}{N^2}\right)dxdydz = \iiint\frac{g}{\rho_0}\rho'W'dxdydz.$$

The eddies have two sources of kinetic energy. There is the conversion from eddy potential energy by the buoyancy term:

$$C_b = -\iiint\frac{g}{\rho_0}\rho'W'dxdydz \tag{3.11}$$

and the conversion from mean state kinetic energy through the Reynolds stress term:

$$C_r = -\iiint\xi_0U'V'dxdydz. \tag{3.12}$$

The magnitudes of C_b and C_r indicate the relative importance of the convective and shear instabilities to the growth of the waves. In the limit of no mean state shear, the waves grow by the conversion of eddy potential energy into eddy kinetic energy; while in the limit of no mean state stratification, the waves grow by the conversion of mean state kinetic energy into eddy kinetic energy. In the general case, an unstably stratified mean state with horizontal wind-shear, both contribute to the growth of the waves.

3. Results

In general the eigenvalue problem (3.9) and (3.10) has no closed form solution and it must be solved numerically. However, it is possible to solve the problem analytically in the pure convective case and the pure shear case. In addition to the solutions in the two limiting cases, there is also an asymptotic solution present for unstably stratified mean states with shear.

In the convective limit, the dispersion relation is

$$\omega^2 = \frac{\lambda^2 f_0^2 - N_s^2(K^2 + l^2)}{K^2 + l^2 + \lambda^2}. \tag{3.13}$$

The wavenumber in the cross-frontal direction K is given by

$$\frac{K(K_1 + K_3)}{K^2 - K_1K_3} = \tan 2Ka. \tag{3.14}$$

By inspection, (3.14) has roots near

$$K \approx \frac{n\pi}{2a},$$

and as a result, the dispersion relation has multiple solutions. There is a branch of solutions with one cell across the convective region, the G_1 mode with $K \approx \pi/2a$; a branch with two cells, the G_2 mode with $K \approx \pi/a$ and so on. As the horizontal scale of the waves decreases, the growth rate asymptotically approaches N_s. In Fig. 2, the growth rates as a function of the horizontal wavenumber for the first two gravity modes are displayed. The growth rate $\sigma(I_m\omega)$ is scaled by the magnitude of the unstable Brunt-Väisälä frequency N_s, while the horizontal wavenumber l is scaled by $a/2\pi$. The phase speed of the waves is zero. The eigenfunc-

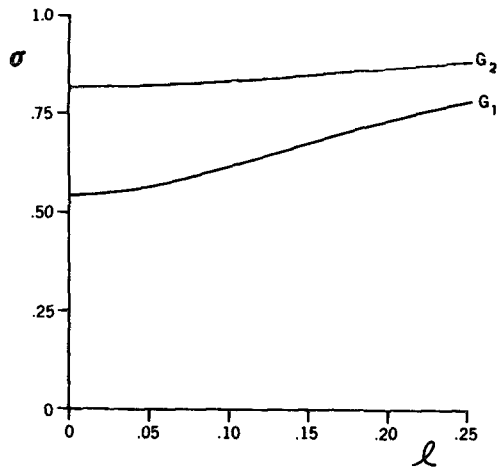

FIG. 2. Nondimensional growth rate $\sigma(I_m\omega)$ of the first two gravity modes, G_1 and G_2, as a function of normalized horizontal wavenumber l for the case $\zeta_0 = 0$, $H/2a = 1$. See text for normalizations.

tions for a representative G_1 and G_2 solution are displayed in Figs. 3 and 4.

The gravity waves have sufficiently small horizontal scales that the effect of rotation on them is minimal. Inclusion of stably stratified air in the outer region leads to a conversion of eddy kinetic energy into eddy potential energy in these regions. This partially offsets the conversion of eddy potential energy into eddy kinetic energy in the inner region and results in a reduction in the growth rates.

In the pure shear limit, the eigenvalue problem (3.9) and (3.10) reduces to

$$\left.\begin{aligned} &P_{xx} - \frac{i2l\xi_0}{\Gamma} P_x - (l^2 + \lambda^2)P = 0 \\ &P_x(-a) = KP(-a) \\ &P_x(a) = -KP(a) \end{aligned}\right\}, \qquad (3.15)$$

where

$$K = (l^2 + \lambda^2)^{1/2}.$$

The solution of this eigenvalue problem results in the following dispersion relation:

$$\omega^2 = -\frac{\xi_0{}^2 l^2}{2K^2}\left[\left(2Ka - \frac{\tanh(2Ka)}{1 + \tanh(2Ka)}\right) - 2Ka^2\right].$$

For $0 < Ka < 0.64$, $\omega^2 < 0$ and there exists a growing solution with $I_m\omega > 0$ and a decaying solution with $I_m\omega < 0$. For $Ka > 0.64$, $\omega^2 > 0$ and there are two neutral traveling solutions.

Therefore in the pure shear limit, the necessary condition for instability is $[(la)^2 + (\lambda a)^2]^{1/2} < 0.64$. The vertical wavenumber, λa, is fixed by the aspect ratio of the mean state. The smallest aspect ratio satisfying the above is $H/2a \approx 2.5$ and as a result only those mean states with aspect ratios greater than this are barotropically unstable. In other words, the only mean states that are unstable are those where the depth of the region is much greater than its width. Observations indicate that the narrow cold-frontal rainband has an aspect ratio of order unity and therefore it is stable to the pure shear instability. In Fig. 5 the growth rates as a function of horizontal wavenumber for the shear mode are displayed. Also shown is the modification of the growth rates due to rotational effects. The growth rate $\sigma(I_m\omega)$ and the Coriolis parameter are scaled by the magnitude of the shear ξ_0, while the horizontal wavenumber is scaled by $a/2\pi$. The introduction of rotation reduces the growth rates of the shear waves and causes a long wave cut-off to appear. The eigenfunctions for the most unstable shear wave are displayed in Fig. 6. The waves grow by converting mean state kinetic energy into eddy kinetic energy through the Reynolds stress term which is proportional to $-U'V'$. In Fig. 6b this correlation is evident. It should be noted that the discontinuity in Fig. 6b at $x = \pm a$ is the result of a discontinuity in the V' field. The U' field is continuous.

There is also a singular solution to (3.9) and (3.10) not present in either limit described above. If one considers an unstably stratified mean state with small but nonzero horizontal wind-shear, then in the limit of large scale, low frequency waves (3.9) reduces to:

$$P_{xx} - \frac{2il\xi_0}{\Gamma} P_x - (l^2 + \lambda^{*2})P = 0, \qquad (3.16)$$

where

$$\lambda^{*2} = \lambda^2\left(\frac{\xi_0}{N_s}\right)^2 (la)^2.$$

Examination of (3.16) shows that, with λ^* defined as above, it is identical to the differential equation for the barotropic problem, (3.15). In a similar fashion the scaled boundary conditions are identical to the ones for the barotropic problem. For the limiting case under study:

$$\zeta_0 \ll N_s \quad \text{and} \quad l \ll 1/a,$$

and as a result:

$$\lambda^* \ll \lambda.$$

Therefore the presence of horizontal wind-shear in an unstably stratified mean state results in a reduction in the effective vertical wavenumber and hence an increase in the effective aspect ratio. This allows a shear-like mode to exist for stratified mean states that are barotropically stable. An asymptotic expression for the dispersion relation in this limit is:

$$\omega = \pm i\zeta_0(la)\left[\frac{1}{3}\frac{(\lambda a) + 3}{(\lambda a) + 1}\right]^{1/2}.$$

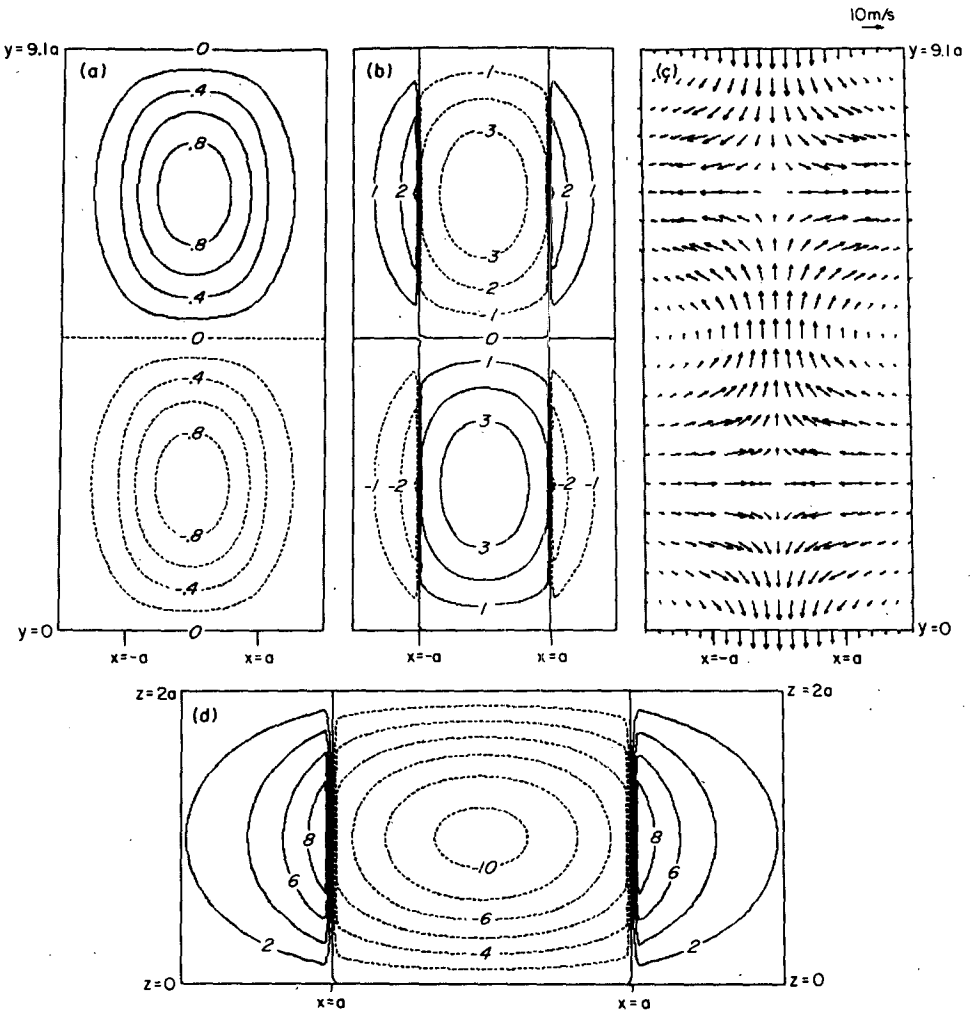

FIG. 3. Horizontal cross sections of (a) the eddy pressure, (b) vertical velocity, (c) horizontal velocity fields and vertical cross section of (d) the vertical velocity field of the G_1 solution for the case $\zeta_0 = 0$, $l = 0.11$ and $H/2a = 1$. The horizontal cross sections are at $z = 0.1H$ and are contoured over one full wavelength in y and over $x = -2a$ to $x = 2a$. The vertical cross section is at $y = 6.8a$ and is contoured over $z = 0$ to $z = H$ and over $x = -2a$ to $x = 2a$. The pressure field is in mb while the velocity fields are in m s^{-1}.

The two solutions form a conjugate pair, a growing solution with $I_m\omega > 0$ and a decaying solution with $I_m\omega < 0$. As the new mode depends critically on the presence of shear in a gravitationally unstable mean state, the solution will be referred to as the shear–gravity mode, or SG_0.

Solutions to the eigenvalue problem (3.9) and (3.10) are required for mean states in which the shear and stratification are both nonzero. The existence of the asymptotic solution gives an indication of the coupling possible when both these instabilities are present. To obtain solutions in this region of interest, the analytic results obtained above were numerically extended by shooting methods described in Moore (1983). Solutions were found as a function of l and ξ_0/N_s. The horizontal wavenumber l was scaled by $a/2\pi$. The ratio ξ_0/N_s determined the relative importance of the two instability mechanisms and its value divided the solutions into two regimes. In the low shear regime, $\xi_0/N_s \leq 0.6$, convective effects dominated and the shear–gravity mode was distinct from the gravity modes. In the high shear regime, $\xi_0/N_s > 0.6$, both the shear and convective effects were important. This resulted in a coupling of the lowest gravity mode and the shear–gravity mode to produce a mixed mode. The aspect ratio of the mean state was fixed at 1. This ensured that the mean state was barotropically stable by the criterion derived before. The analysis was carried out on an irrotational mean state with no stratification in the outer regions. The effects of rotation and outer region stratification were found to be small. For each solution, the eigenfunctions (3.4) were found. This allowed the Reynolds

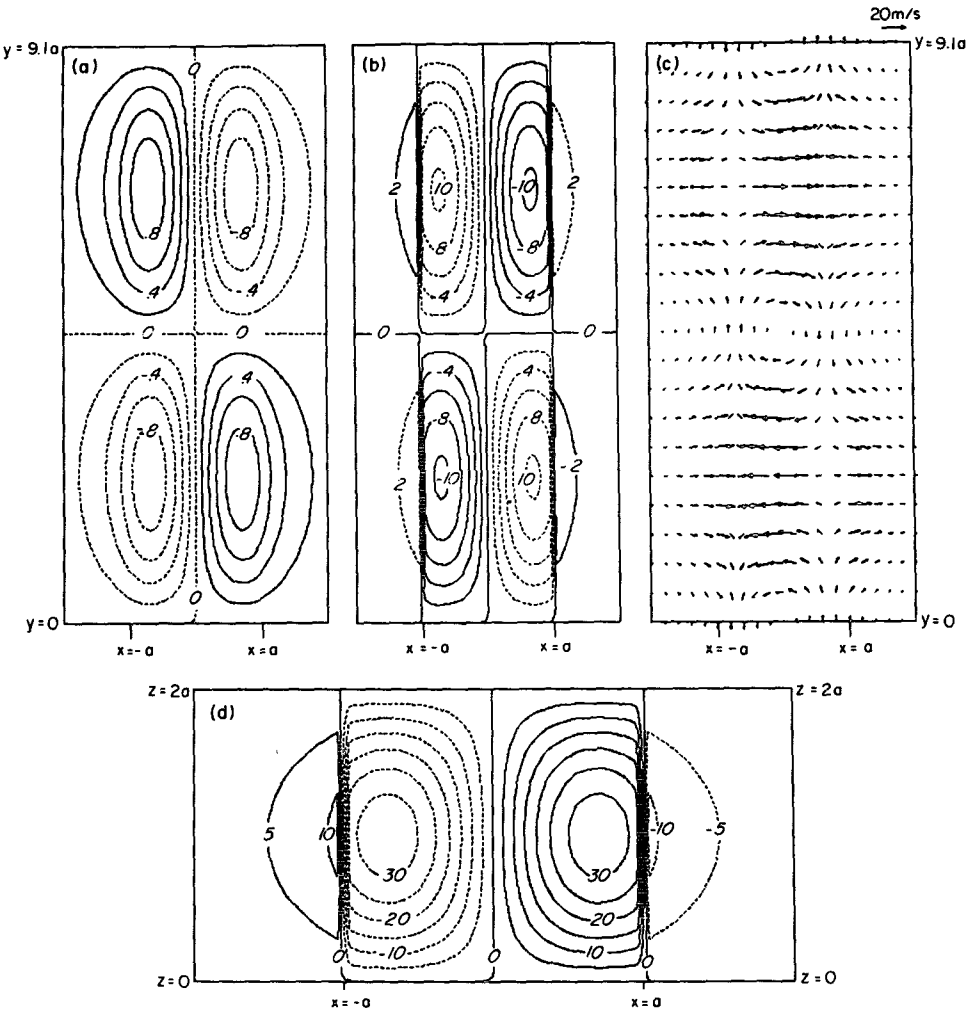

FIG. 4. As in Fig. 3 but for the G_2 solution.

stress and the buoyancy conversion terms, (3.11) and (3.12), to be calculated. They were normalized by the total eddy kinetic energy. The multiplicative constant in the magnitudes of the eigenfunctions was removed by setting the maximum pressure perturbation to 1 mb.

Figures 7 and 8 show the growth rates and energy conversion terms for the first two gravity modes and the shear gravity mode for $\xi_0/N_s = 0.5$, a representative mean state in the low shear regime. For the gravity modes, the introduction of shear resulted in modifications in the efficiency of the waves at releasing the energy stored in the unstably stratified mean state. The long waves had marginally smaller growth rates than in the no shear limit, while the short waves had much higher ones. Figure 9 shows the eigenfunctions of a typical G_1 solution. With the introduction of shear into the mean state, the waves had a nonzero Reynolds stress term. However, it was small compared with the buoyancy term. In the low shear regime, the shear–gravity mode was isolated. In the intermediate wavelength region, the Reynolds stress term had a maximum indicating a preferred length scale for the conversion of mean state kinetic energy into eddy kinetic energy. In this region the buoyancy conversion term was small compared to C_r. In the short wavelength limit, the waves became inefficient at shear conversion but more efficient at buoyancy conversion. The cutoff was the result of the inability of the mean state to support short shear waves. Figure 10 shows the eigenfunctions associated with the most unstable SG_0 wave for $\xi_0/N_s = 0.5$.

Comparison of the eigenfunctions associated with the solutions in the G_1 and SG_0 modes, Figs. 9 and 10, show that in both cases the pressure field has a distinct phase tilt of $\sim 30°$. The horizontal velocity field of both solutions shows cyclonic curvature with regions of flow into and out of the frontal zone. In the G_1 solution,

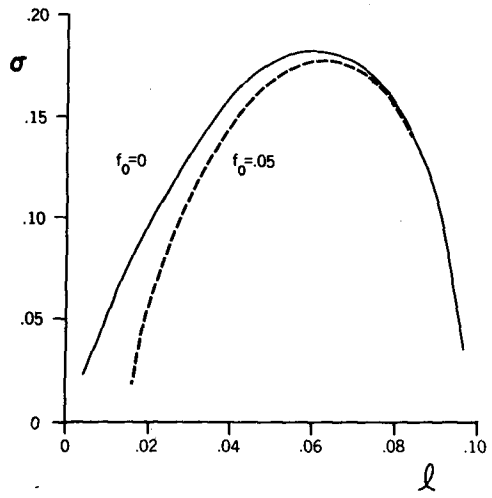

FIG. 5. Nondimensional growth rate $\sigma(I_m\omega)$ of the shear mode as a function of normalized horizontal wavenumber l for the case $N_s = 0$, $H/2a = 10$. The curves are labeled with values of the nondimensional Coriolis parameter f_o. See text for normalizations.

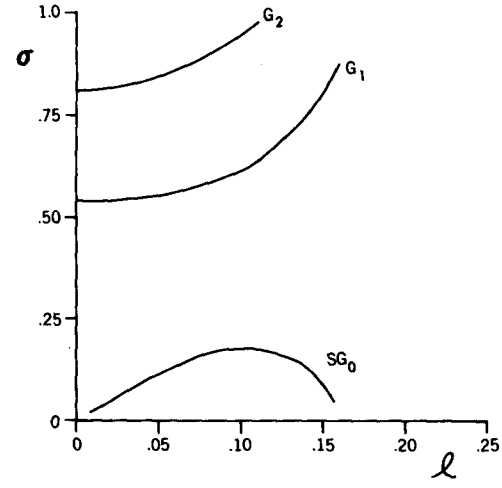

FIG. 7. Nondimensional growth rate $\sigma(I_m\omega)$ of the shear–gravity mode, SG_0 and the first two modified gravity modes, G_1 and G_2, as a function of normalized horizontal wavenumber l for the case $\xi_0/N_s = 0.5$ and $H/2a = 1$. See text for normalizations.

these are associated with areas of convergence and divergence; while in the SG_0 solution, the interior flow is quasi-nondivergent and W' is small. There is a strong correlation between U' and V' evident in the SG_0 solution, it is not present in the G_1 solution. Thus examination of the eigenfunctions emphasizes the fact that the G_1 mode is dominated by the convective instability while the SG_0 mode is dominated by the shear instability.

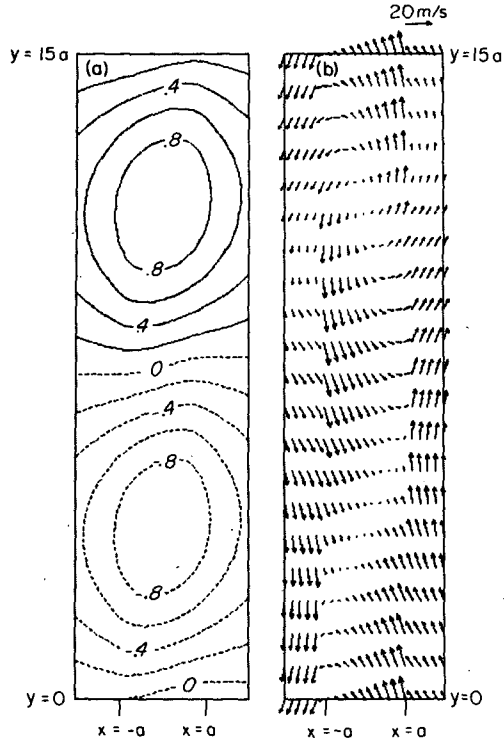

FIG. 6. Horizontal cross sections of (a) the eddy pressure and (b) horizontal velocity fields of the most unstable shear wave, $N_s = 0$, $l = 0.065$, $H/2a = 10$. The fields are contoured as in Fig. 3.

As ξ_0/N_s was increased above 0.6, there was an abrupt change in the character of the solutions. Figs. 11 and 12 show the growth rates, phase speeds and energy conversion terms for $\xi_0/N_s = 0.8$, a representative mean state in the high shear regime. For the intermediate scale waves, the SG_0 and the G_1 modes merged to form a doublet with the same growth rate but equal and opposite phase speeds. Examination of Fig. 12 shows that for the waves in this doublet, the buoyancy conversion term and the Reynolds stress conversion term are of the same order. Recall that the conversion of eddy potential energy into eddy kinetic energy favours those waves with the smallest length scales, while the conversion of mean state kinetic energy into eddy kinetic energy has a preferred intermediate length scale. Thus the doublet exists only for those waves that are "short" enough for the convective instability and "long" enough for the shear instability. The SG_0 mode had a short wave cutoff that existed regardless of the enhanced buoyancy conversion of the waves and near this cut-off, the doublet separated. At bifurcation, the phase speed returned to zero. Examination of the eigenfunctions of the most unstable solution of the $SG_0 - G_1$ doublet, Fig. 13, shows the same cyclonic curvature and regions of convergence and divergence that were present in the G_1 solution in the low-shear regime, Figs. 9b and 9c, and the correlation between U' and V' that was present in the SG_0 solution in the low-shear regime, Fig. 10c. This indicates that both the Reynolds stress and buoyancy conversion term contribute to the

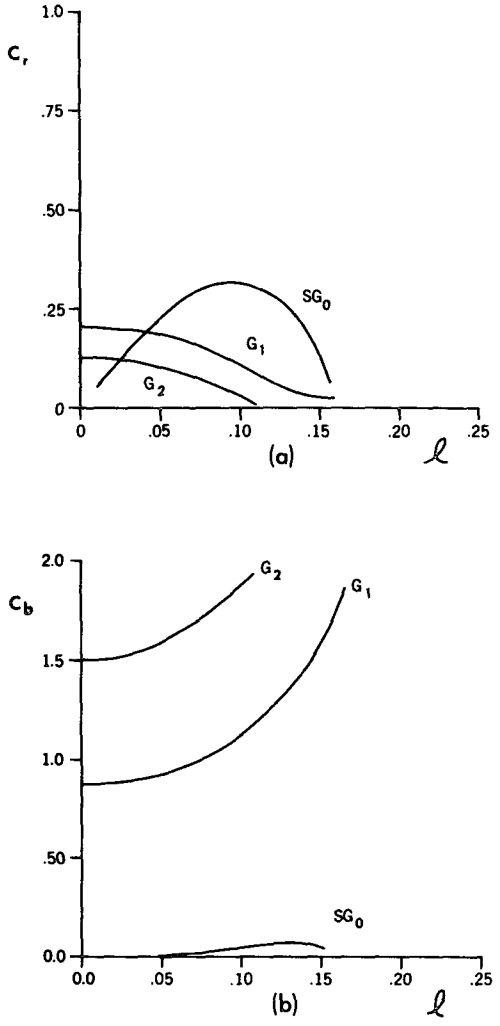

FIG. 8. (a) Nondimensional Reynolds stress conversion term C_r and (b) buoyancy conversion term C_b of the shear–gravity mode SG_0 and the first two modified gravity modes, G_1 and G_2, as a function of normalized horizontal wavenumber l for the case $\xi_0/N_s = 0.5$ and $H/2a = 1$. See text for normalizations.

growth of the waves in this doublet. In addition, the W' field is more realistic than that for either solution in the low-shear regime.

As in the analytic solutions described earlier, inclusion of rotation reduced the growth rates of the long waves. Inclusion of stably stratified air in the outer regions resulted in a decrease in the growth rates of all the waves. These effects were most pronounced in the shear–gravity mode where a long wave cut-off appeared. Figure 14 shows the growth rates of the shear–gravity mode as a function of Coriolis parameter and outer region stratification.

In summary, the introduction of horizontal windshear into the model resulted in modifications to the gravity modes and enabled a solution to exist that was not present in the convective limit. The primary effect of shear on the gravity modes was to reorient them so as to change their efficiency at converting eddy potential energy into eddy kinetic energy. The direct conversion of mean state kinetic energy into eddy kinetic energy was small. For the long waves, this resulted in a decrease in the growth rates as compared to the no shear case. For intermediate and short waves, the reorientation resulted in an increase in the growth rates. The shear–gravity mode was similar to the mode in the pure shear case, however it existed for mean states that were barotropically stable. Both the Reynolds stress and buoyancy conversion terms contributed to the growth of the shear–gravity waves. As the mean state shear increased, the intermediate scale G_1 and SG_0 waves formed a doublet with the same growth rate but opposite phase speeds. The energetics showed that the buoyancy and Reynolds stress terms were the same size for this mixed mode.

4. Discussion

Examination of the growth rates obtained show that the most unstable waves in the model were the very short scale gravity waves. In the convective limit, all of the waves in a given mode had the same cross-frontal structure, while in the mean states with shear it was a function of wavenumber. As the shear increased, the cells became elongated and narrow. This is indicated in Fig. 15, where the eddy vertical velocity as a function of shear and wavenumber is shown. As remarked in Section 3, the growth rates of the small scale waves in the gravity modes were much larger in mean states with shear. This was the result of the very small cross-frontal scales that led to a greatly increased efficiency at buoyancy conversion. The model is inviscid and as discussed by Lilly (1960), inclusion of viscosity, diffusion and entrainment effects would suppress the explosive growth of these small scale waves. In this inviscid model, the problem arises of how to separate the shear-induced organization of the convection from the highly unstable small-scale solutions. Kuo (1963) in his study of the stability of Couette flow in a stratified fluid encountered a similar difficulty. Not wanting to solve the complete viscous problem, he included a dissipative term that damped the growth of the waves with scales smaller than those assumed to be of interest. Rather than using an *ad hoc* dissipative term, I will instead *a posteriori* reject all solutions with cross-frontal scales much less than the width of the frontal zone. As the model is used to study the organization of convection along the band, no assumptions are made about the scales of the solutions in this direction. Use of the gravest mode hypothesis eliminates all solutions in the G_2 and higher gravity modes and the short waves in the G_1 mode for mean states with shear. An example of such a rejected solution is the $l = 0.18$ wave shown in Fig. 15d. It has a very small cross-frontal scale and

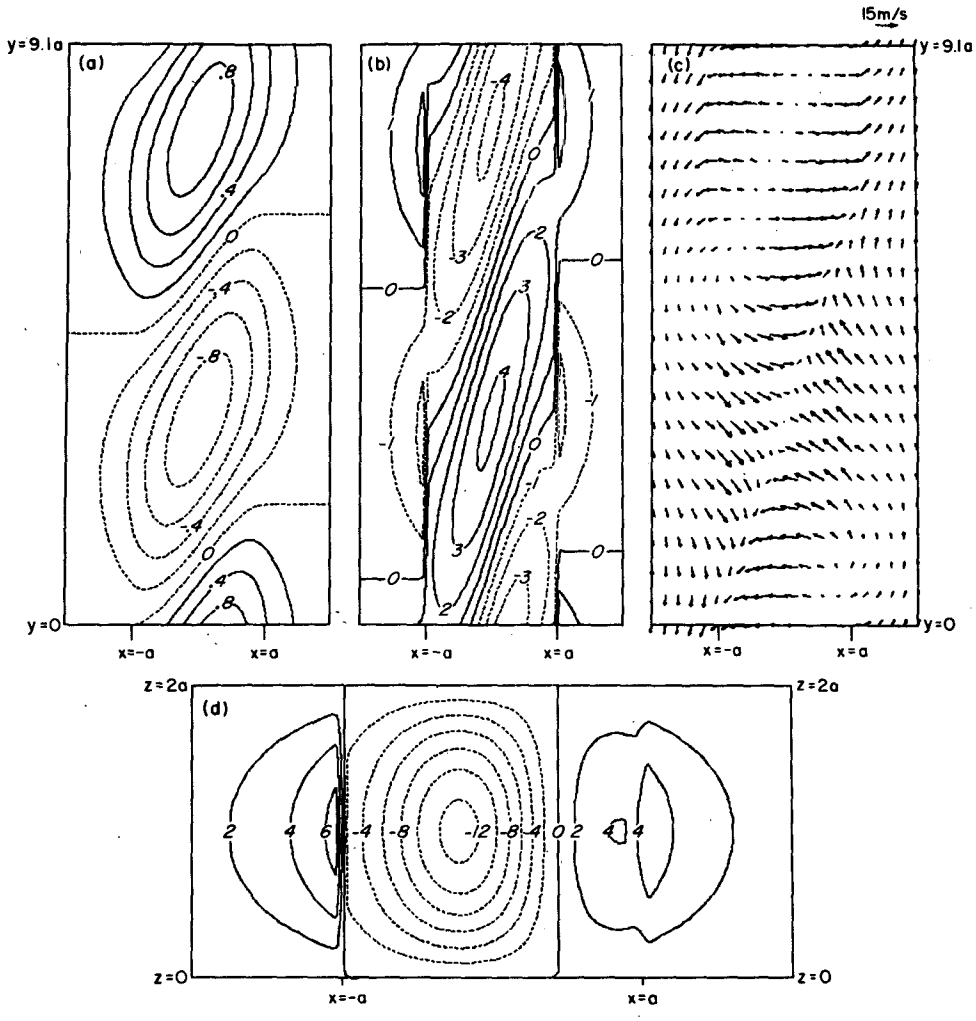

FIG. 9. Horizontal cross sections of (a) the eddy pressure, (b) vertical velocity, (c) horizontal velocity fields and vertical cross section of (d) the vertical velocity field of the modified G_1 solution for the case $\xi_0/N_s = 0.5$, $l = 0.11$, $H/2a = 1$. The fields are contoured as in Fig. 3.

very large vertical velocities and would be strongly damped by inclusion of viscous effects. The elimination of the solutions with very small cross-frontal scales allows the results of the inviscid linear stability analysis to be used to study the shear-induced organization of convection in the narrow cold-frontal rainband.

To fix the dimensional parameters that define the mean state, the observations described in Section 1 were used. The width $2a$ and height H of the frontal zone were set at 5 km. The magnitude of the shear across the zone ξ_0 was 3×10^{-3} s^{-1}. This corresponds to a change of 15 m s^{-1} in the along front velocity field across the band. The air outside the frontal zone was assumed to be neutrally stratified and the Coriolis parameter was set to zero. The parameterization of the convective processes is fixed by the magnitude of the unstable Brunt-Väisälä frequency and it is not readily obtained from the observations upon which the other parameters were set. Based on observation and calculations detailed in Lilly (1960), a value for N_s of 4 $\times 10^{-3}$ s^{-1} was used. Narrow cold-frontal rainbands are characterized by aspect ratios of order one. That is, the depth of the convection is commensurate with its width, and as a result they are barotropically stable. The relatively small aspect ratio of the narrow cold-frontal rainband separates it from other atmospheric phenomena with large aspect ratios, such as shear lines and gust fronts, that may be barotropically unstable. As was shown in Section 3, the behavior of the solutions depended primarily on the ratio ξ_0/N_s and for values of it above 0.6, there was a mixed mode present that was the result of a coupling between shear and convective instabilities. From the preceding, the narrow cold-frontal rainband has $\xi_0/N_s \sim 0.8$ and hence it is

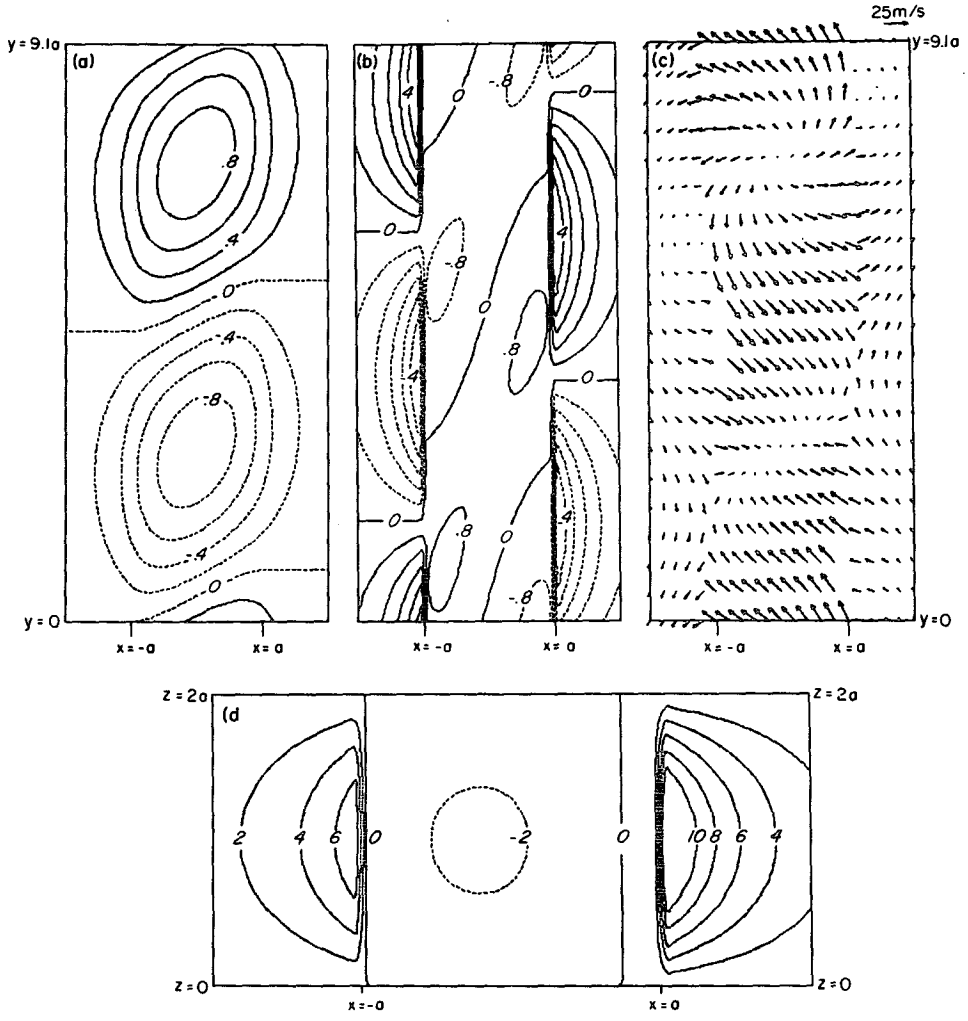

FIG. 10. As in Fig. 9 but for the most unstable shear–gravity wave.

in the regime where the mixed mode is present. I will discuss the results by considering three different unstably stratified mean states, one with no shear present, one in the low shear regime and one in the high shear regime. It is this final case that is applicable to the narrow cold-frontal rainband. In all cases, only those solutions which satisfy the gravest mode hypothesis will be considered.

For the mean state without shear, the only mode present is the first gravity mode. All the waves in the G_1 mode had the unicellular structure displayed in Fig. 3. They are strongly three-dimensional with regions of inflow and outflow associated with cores of ascending and descending motion. The flow is irrotational. For this mode, the growth rate increases as the scale of the waves decreases and there is no preferred scale for the growth of the eddies.

In the low shear regime, the G_1 and the SG_0 modes satisfy the gravest mode hypothesis. The structure of the waves in these modes is a function of wavenumber. Comparison of Figs. 3 and 9 show that the waves in the G_1 mode with shear have the same basic structure as in the solutions without shear, the only difference being a phase tilt of $\approx 30°$ that was present. The SG_0 mode, Fig. 10, is characterized by its quasi-nondivergent interior flow with a strong correlation between U' and V'. The shear–gravity mode has a preferred scale for the growth of the eddies. For the modified gravity mode, the growth rate increases as the scale of the waves decreases. The higher growth rates are associated with the modified gravity mode. As the wavenumber increased, the cross frontal scale of the waves in the G_1 mode became smaller. Based on the growth rates, there is no distinct transition from allowable solutions to

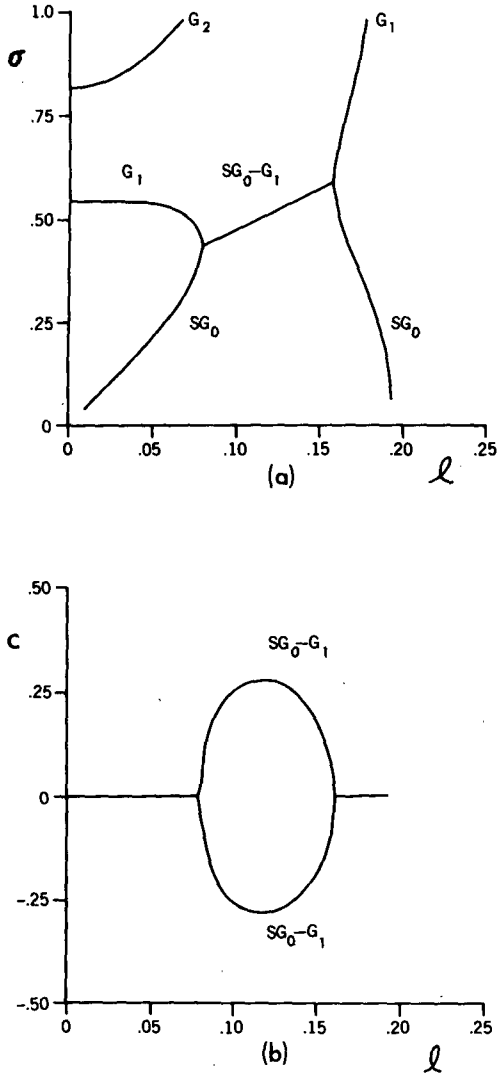

FIG. 11. (a) Nondimensional growth rate $\sigma(I_m\omega)$ and (b) phase speed $c(R_e\omega/l)$ of the shear–gravity mode SG_0 and the first two modified gravity modes, G_1 and G_2, as a function of normalized horizontal wavenumber l for the case $\xi_0/N_s = 0.8$ and $H/2a = 1$. See text for normalizations.

those that violate the gravest mode hypothesis and as a result it is difficult to identify a most unstable wave. Although there is a mode present with a short wave cut-off, the low shear regime is still dominated by gravitational effects and as a result there is no preferred scale for the organization of the convection.

For the mean state in high shear regime, the intermediate scale waves in the G_1 and SG_0 modes form a doublet with equal growth rates but opposite phase speeds. All of the waves in this mixed mode satisfy the gravest mode hypothesis. There is an abrupt transition in the structure of the solutions at the separation wavenumber of the doublet. After separation, the cross-frontal scale of the short gravity waves becomes very small and they violate the gravest mode hypothesis. Ignoring these highly unstable solutions, the largest growth rates occur for the very long gravity waves and for waves in the mixed mode. The gravity waves with scales of order 100 km act to modulate the 10–15 km mixed mode waves. The narrow cold-frontal rainband is in the high shear regime and the eigenfunctions of the most unstable wave (Fig. 13) show many features reminiscent of precipitation cores. There are strong regions of inflow and outflow associated with cores of ascending and descending air. The regions of strongest convergence are along the leading edge of the front. Although the model has no precipitation parameter-

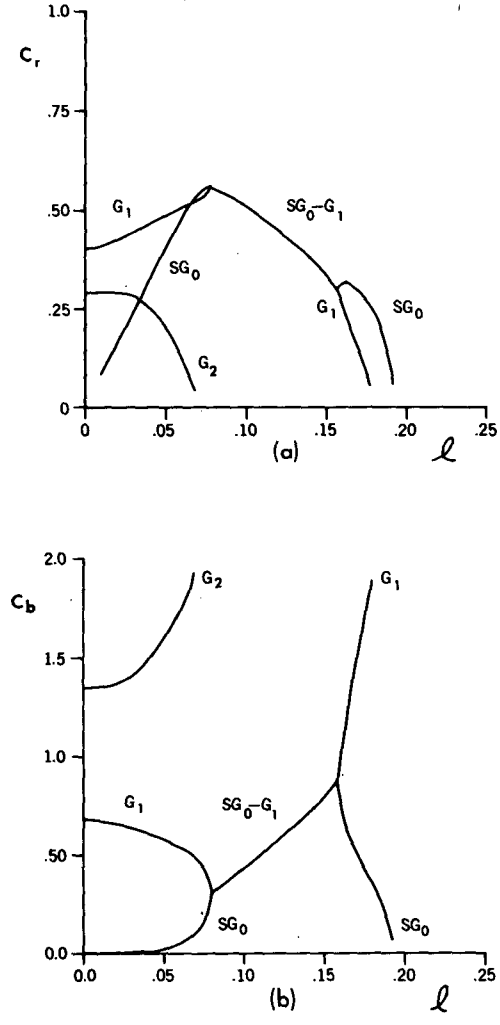

FIG. 12. (a) Nondimensional Reynolds stress conversion term C_r and (b) buoyancy conversion term of the shear–gravity mode SG_0 and the first two modified gravity modes, G_1 and G_2, as a function of normalized horizontal wavenumber l for the case $\xi_0/N_s = 0.8$ and $H/2a = 1$. See text for normalizations.

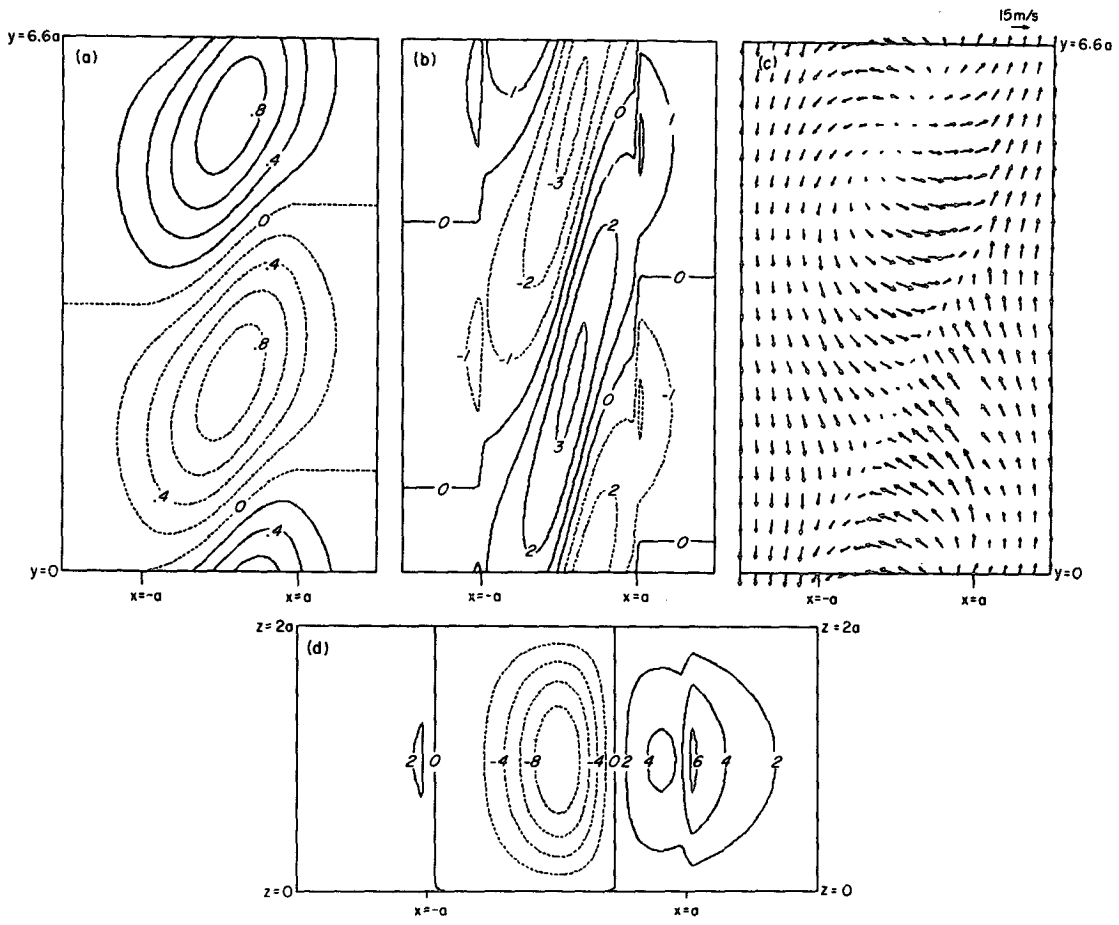

FIG. 13. As in Fig. 9 but of the most unstable $SG_0 - G_1$ wave, $\xi_0/N_s = 0.8$, $l = 0.15$, $H/2a = 1$. The fields are contoured as in Fig. 3 with the exception that the vertical cross-section is at $y = 5a$.

ization in it, one may consider the ascending cores as regions where rain would be expected and the descending ones as regions free of rain. As remarked in Section 2, the mean state has no vertical wind-shear and as a result the ascending and descending regions have no vertical slant. These cores have a characteristic horizontal tilt of 30° with respect to the front. The wavelength of the most unstable wave is approximately 15 km and the time required for it to double in amplitude is approximately 8 min. Examination of Fig. 11 shows that near the most unstable wave in the mixed mode, the phase speeds are almost zero. Hence the most unstable wave can be considered to be stationary with respect to the front. All of these values are consistent with the observations described in Section 1 and indicate that a coupling of shear and convective instabilities may be responsible for the organization of convection in the narrow cold-frontal rainband.

Acknowledgments. This paper is based on part of my Ph.D. thesis completed while associated with the Geophysical Fluid Dynamics Program at Princeton

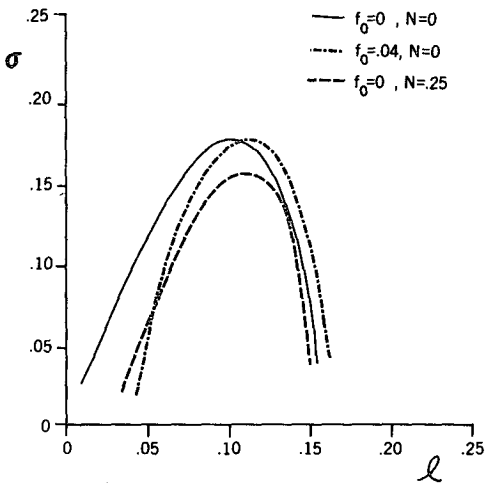

FIG. 14. Nondimensional growth rate $\sigma(I_m\omega)$ of the shear–gravity mode as a function of nondimensional horizontal wavenumber for the case $\xi_0/N_s = 0.5$ and $H/2a = 1$. The curves are labeled with values of the nondimensional Coriolis parameter and the nondimensional outer region Brunt-Väisälä frequency. See text for normalizations.

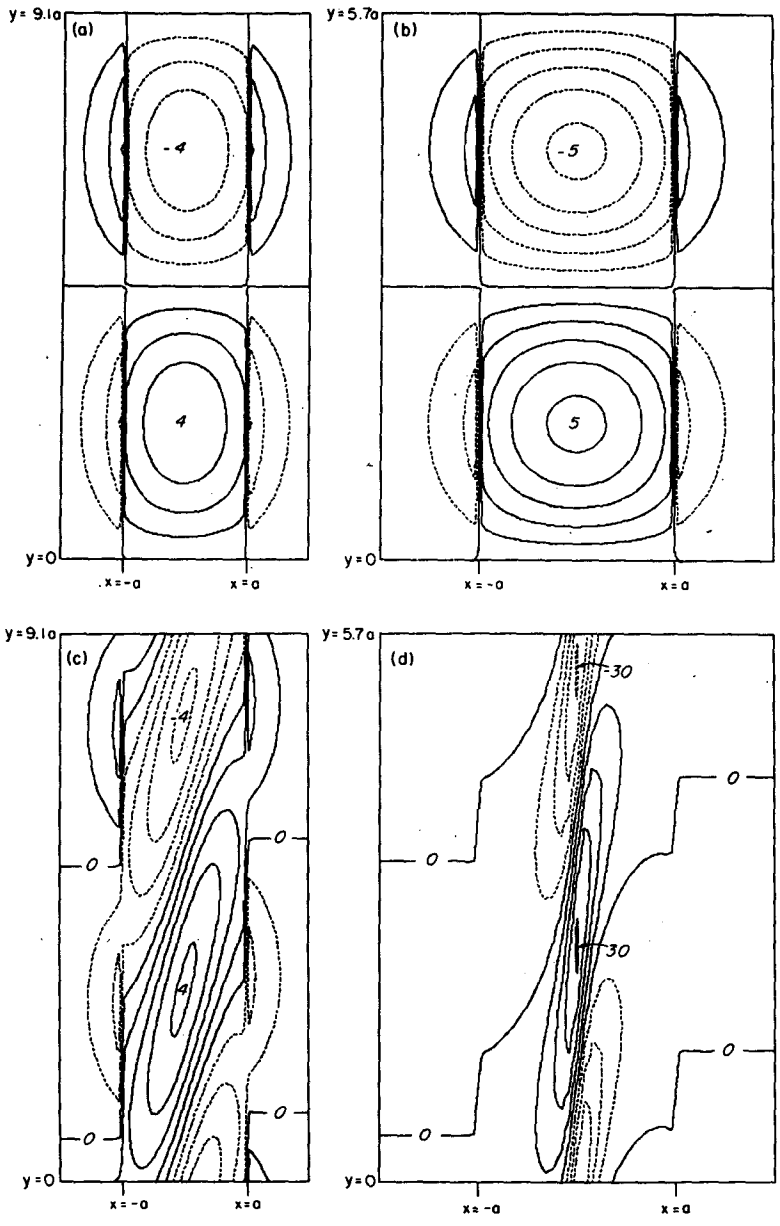

FIG. 15. Horizontal cross sections of the vertical velocity fields of the G_1 mode as a function of nondimensional wavenumber l and shear parameter ξ_0/N_s. Panel (a): $\xi_0/N_s = 0$ and $l = 0.11$. Panel (b): $\xi_0/N_s = 0$ and $l = 0.18$. Panel (c): $\xi_0/N_s = 0.5$ and $l = 0.11$. Panel (d): $\xi_0/N_s = 0.5$ and $l = 0.18$. The fields are contoured as in Fig. 3.

University. I would like to thank my advisor, Dr. I. Orlanski, for his suggestion of the problem and for his guidance during the course of my investigation and the reviewers for their comments. Financial support was provided by the Natural Sciences and Engineering Research Council of Canada. I would like to thank K. Khan for drafting the figures and A. Sousa for typing the manuscript.

REFERENCES

Barcilon, A., and P. G. Drazin, 1972: Dust devil formation. *Geophys. Fluid Dyn.*, **4**, 147–157.

Carbone, R. E., 1982: A severe winter squall line: Stormwide hydrodynamic structure. *J. Atmos. Sci.*, **39**, 258–279.

Emanuel, K. A., 1980: Forced and free mesoscale motions in the atmosphere. *Collection of Lecture Notes on Dynamics of Mesometeorological Disturbances. Proc. Cimms Symposium*, University of Oklahoma Press, 191–259.

Hobbs, P. V., 1978: Organization and structure of clouds and precipitation on the mesoscale and microscale in cyclonic storms. *Rev. Geophys. Space Phys.*, **16**, 741–755.

——, and K. R. Biswas, 1979: The cellular structure of the narrow cold-frontal rainbands. *Quart. J. Roy. Meteor. Soc.*, **105**, 723–727.

——, and P. O. G. Persson, 1982: The mesoscale and microscale structure and organization of clouds and precipitation in midlatitude cyclones. Part V: The substructure of narrow cold-frontal rainbands. *J. Atmos. Sci.*, **39**, 280–295.

James, P. K., and K. A. Browning, 1979: Mesoscale structure of line convection at surface cold fronts. *Quart. J. Roy. Meteor. Soc.*, **105**, 371–382.

Kuo, H. L., 1963: Perturbations of plane couette flow in a stratified fluid and origin of cloud streets. *Phys. Fluids*, **6**, 195–211.

Lilly, D. K., 1960: On the theory of disturbances in a conditionally unstable atmosphere. *Mon. Wea. Rev.*, **88**, 1–17.

Matejka, T. J., 1980: Mesoscale organization of cloud processes in extratropical cyclones. Ph.D. thesis, University of Washington, 361 pp.

——, R. A. Houze and P. V. Hobbs, 1980: Microphysics and dynamics of clouds associated with mesoscale rainbands in extratropical cyclones. *Quart. J. Roy. Meteor. Soc.*, **106**, 29–56.

Moore, G. W. K., 1983: On the structure of the narrow cold-frontal rainband. Ph.D. thesis, Princeton University, 141 pp.

Orlanski, I., and B. B. Ross, 1984: The evolution of an observed cold front. Part II: Mesoscale dynamics. *J. Atmos. Sci.*, **41**, 1669–1703.

Parsons, D. B., and P. V. Hobbs, 1983: The mesoscale and microscale structure and organization of clouds and precipitation in midlatitude cyclones. Part VII: Formation, development interaction and dissipation of rainbands. *J. Atmos. Sci.*, **40**, 559–579.

Ross, B. B., and I. Orlanski, 1982: The evolution of an observed cold front. Part I: Numerical simulation. *J. Atmos. Sci.*, **39**, 296–327.